






RESEARCH ARTICLE | DECEMBER 08 2020

Nonvolatile manipulation of electronic and ferromagnetic properties of NiO–Ni epitaxial film by ferroelectric polarization charge

Ming-Yuan Yan; Jian-Min Yan ; Meng-Yuan Zhang; Ting-Wei Chen; Guan-Yin Gao; Fei-Fei Wang ; Yang Chai ; Ren-Kui Zheng  



Appl. Phys. Lett. 117, 232901 (2020)

<https://doi.org/10.1063/5.0025335>



Articles You May Be Interested In

Nonvolatile transtance change random access memory based on magnetoelectric P(VDF-TrFE)/Metglas heterostructures

Appl. Phys. Lett. (December 2016)

Voltage-impulse-induced dual-range nonvolatile magnetization modulation in metglas/PZT heterostructure

Appl. Phys. Lett. (November 2016)

Effect field controlled magnetization in NiFe₂O₄/SrRuO₃/PMN-PT heterostructures for nonvolatile memory applications: XMCD study

Appl. Phys. Lett. (September 2021)



Applied Physics Letters

Special Topics Open for Submissions

[Learn More](#)

Nonvolatile manipulation of electronic and ferromagnetic properties of NiO–Ni epitaxial film by ferroelectric polarization charge

Cite as: Appl. Phys. Lett. **117**, 232901 (2020); doi: [10.1063/5.0025335](https://doi.org/10.1063/5.0025335)

Submitted: 14 August 2020 · Accepted: 13 November 2020 ·

Published Online: 8 December 2020



View Online



Export Citation



CrossMark

Ming-Yuan Yan,^{1,2} Jian-Min Yan,² Meng-Yuan Zhang,¹ Ting-Wei Chen,³ Guan-Yin Gao,⁴ Fei-Fei Wang,^{1,a)} Yang Chai,⁵ and Ren-Kui Zheng^{2,3,a)}

AFFILIATIONS

¹Key Laboratory of Optoelectronic Material and Device, Department of Physics, Shanghai Normal University, Shanghai 200234, China

²State Key Laboratory of High Performance Ceramics and Superfine Microstructure, Shanghai Institute of Ceramics, Chinese Academy of Sciences, Shanghai 200050, China

³School of Materials Science and Engineering, Nanchang University, and Jiangxi Engineering Laboratory for Advanced Functional Thin Films, Nanchang 330031, China

⁴Hefei National Laboratory for Physical Sciences at the Microscale, University of Science and Technology of China, Hefei 230026, China

⁵Department of Applied Physics, The Hong Kong Polytechnic University, Hong Kong, China

^{a)}Authors to whom correspondence should be addressed: ffwang@shnu.edu.cn and zrk@ustc.edu

ABSTRACT

NiO–Ni composite films were heteroepitaxially grown on (111)-oriented ferroelectric 0.31Pb(In_{1/2}Nb_{1/2})O₃–0.35Pb(Mg_{1/3}Nb_{2/3})O₃–0.34PbTiO₃ (PIN–PMN–PT) single-crystal substrates by pulsed laser deposition. The NiO films prepared in high vacuum are *n*-type conducting and possess room-temperature ferromagnetism, which originates from oxygen vacancies and the presence of the second Ni phase, respectively. Taking advantage of the electric-field-induced ferroelectric polarization charges, we realized *in situ* reversible and nonvolatile modulation of both the electrical resistance and magnetism of the film. A relative resistance change of ~470% is obtained at room temperature, while an appreciable magnetization change of ~15% was achieved at 50 K by switching the polarization states of PIN–PMN–PT. The coexistence of charge-density-tunable electronic and magnetic properties of NiO–Ni/PIN–PMN–PT heterostructures may provide a strategy to design charge-mediated multiferroic devices for nonvolatile memory and spintronic applications.

Published under license by AIP Publishing. <https://doi.org/10.1063/5.0025335>

With the increasing demand for multilevel memories with high density, low power consumption, and good stability, constructing multiferroic heterostructures and spintronic devices is currently attracting considerable attention.^{1–3} For the former purpose, numerous functional thin films, such as colossal magnetoresistive manganites,⁴ superconductors,⁵ multiferroic bismuth ferrites,⁶ photoluminescence oxides,⁷ ferromagnetic ferrites,⁸ topological insulators,⁹ and two-dimensional materials, have been directly grown on Pb(Mg_{1/3}Nb_{2/3})O₃–PbTiO₃ (PMN–PT) ferroelectric (FE) single-crystal substrates to form heterostructures.¹⁰ An electric-field-manipulation of optical, electrical, or magnetic properties of these films has been achieved through lattice-strain and/or interfacial charge-mediated coupling. Unfortunately, the electric-field-induced nonvolatile lattice strain is usually unstable and small in

magnitude, which is unfavorable for practical device applications.^{11–15} In contrast, the interfacial charge effects, i.e., ferroelectric field effect, can stably and drastically adjust the resistance of films due to the remnant polarization charges of PMN–PT,^{16,17} which offers a straightforward approach to achieve dynamic nonvolatile modulation of physical properties.

Alternatively, high storage performance and low loss spin devices can also be realized by utilizing room-temperature ferromagnetic semiconductors.^{18,19} Seeking for candidate semiconductor materials with room temperature ferromagnetic properties is highly desired for the development of spintronics. To achieve this goal, the so-called diluted magnetic semiconductors (DMSs),²⁰ coexistence of ferromagnetism and semiconducting, can be realized by doping magnetic

elements into nonmagnetic semiconductors, exemplified by ZnO-based,²¹ TiO₂-based,²² SnO₂-based,²³ NiO-based,^{24,25} and other oxide-based materials.²⁶ Among those widely investigated DMSs, NiO, a wide-bandgap oxide semiconductor ($E_g = 3.6\text{--}3.8\text{ eV}$), shows room temperature ferromagnetism by magnetic element (Fe, Co) doping or ionic liquid gating.^{24,25,27} However, NiO-based materials have been extensively studied as resistive random access memory (RRAM) for their resistive switching effects in previous investigations.²⁸ Besides, several studies on NiO film/PMN-PT heterostructures mainly focused on exchange bias effects.²⁹ As of now, there are a few reports that the electrical, magnetic, and other properties of NiO-based multiferroic heterostructures have been nonvolatily modulated by external perturbations. Therefore, an experimental investigation of NiO/FE heterostructures is needed to realize reversible and nonvolatile modulation of resistance and ferromagnetism simultaneously, thus promoting their potential applications in memory and spintronic devices.

Similar to PMN-PT, the perovskite $0.31\text{Pb}(\text{In}_{1/2}\text{Nb}_{1/2})\text{O}_3\text{--}0.35\text{Pb}(\text{Mg}_{1/3}\text{Nb}_{2/3})\text{O}_3\text{--}0.34\text{PbTiO}_3$ (PIN-PMN-PT) FE single crystal with a pseudocubic structure also exhibits superior piezoelectric and ferroelectric responses near the morphotropic phase boundary (MPB), which can be selected as a FE substrate to tune the properties of functional films.³⁰ Moreover, bulk NiO has a cubic phase at room temperature, which makes it possible for NiO films to grow epitaxially on PIN-PMN-PT substrates. Furthermore, the volume carrier concentration of bulk NiO is generally on the order of 10^{14} cm^{-3} , and the corresponding areal carrier density of NiO films is much lower than the surface charge density of PIN-PMN-PT ($2 \times 10^{14}\text{ charges/cm}^2$),³¹ which enables NiO films to be an ideal candidate for integration on PIN-PMN-PT. Therefore, it is expected that NiO/PIN-PMN-PT heterostructures can achieve large reversible and nonvolatile modulation of the physical properties of NiO films utilizing polarization charges of PIN-PMN-PT.

In this Letter, through pulse laser-ablating the NiO target in high vacuum ($5.0 \times 10^{-4}\text{ Pa}$), we fabricated heteroepitaxial NiO–Ni composite films on PIN-PMN-PT (111) single-crystal substrates and realized *in situ* modulation of two resistance states in a reversible and nonvolatile manner via interfacial charge effects. A relative resistance change ($\Delta R/R$) of the NiO–Ni composite film up to $\sim 470\%$ with excellent stability was achieved at 300 K. Particularly, the NiO films deposited in high vacuum possess room-temperature ferromagnetism, which arises from the presence of the Ni phase.

NiO–Ni composite films were deposited on one-side polished (111)-oriented $0.31\text{Pb}(\text{In}_{1/2}\text{Nb}_{1/2})\text{O}_3\text{--}0.35\text{Pb}(\text{Mg}_{1/3}\text{Nb}_{2/3})\text{O}_3\text{--}0.34\text{PbTiO}_3$ (PIN-PMN-PT) single crystal substrates with a dimension of $5\text{ mm} \times 5\text{ mm} \times 0.5\text{ mm}$ via the pulse laser deposition (PLD) using a XeCl excimer laser ($\lambda = 308\text{ nm}$). During film deposition, the substrate temperature, pressure, target-to-substrate distance, laser energy density, and pulse repetition rate were kept at 600°C , $5.0 \times 10^{-4}\text{ Pa}$, 5 cm , 2 J/cm^2 , and 3 Hz , respectively. After *in situ* annealing for 30 min, the as-grown films were cooled to room temperature at a rate of 5°C/min .

The phase purity and epitaxial properties of the as-grown films were analyzed by X-ray diffraction (XRD) θ – 2θ and φ scans, respectively, using a PANalytical X'Pert PRO x-ray diffractometer with CuK α 1 radiation ($\lambda = 1.5406\text{ \AA}$). The thickness and composition of films were measured using a Tecnai G2 F20 S-Twin transmission electron microscope (TEM). The chemical valence states of the Ni element

were analyzed by X-ray photoelectron spectroscopy (XPS). The surface morphology of films and piezoelectric properties of PIN-PMN-PT substrates were characterized by atomic force microscopy (AFM) and piezoresponse force microscopy (PFM), respectively, using a MFP-3D Infinity atomic force microscope (Oxford Instruments Asylum Research Inc.). The polarization–electric field (P – E) hysteresis loops of PIN-PMN-PT substrates were recorded using a Precision Multiferroic Analyzer (Radiant Technologies, Inc. USA). The electric-field-induced in-plane strain in PIN-PMN-PT substrates was measured using a strain gauge, which was attached to the substrate surface with epoxy [Fig. S1(a), [supplementary material](#)].

The resistance and carrier density of the NiO–Ni composite films were measured through the standard four-probe technique and the van der Pauw method [Fig. S1(b), [supplementary material](#)], respectively, using a physical property measurement system (PPMS-9, Quantum Design). The magnetic properties of the NiO–Ni composite films were measured using a superconducting quantum interference device (SQUID) magnetometer (Quantum Design, MPMS-XL5).

Figure 1(a) shows the XRD θ – 2θ scan pattern of the NiO–Ni film deposited on the PIN-PMN-PT (111) substrate. The pattern indicates that the film is composed of NiO and Ni phases, which are highly (l)-oriented ($l = 1, 2$), suggesting that the film grows heteroepitaxially under this condition. As can be seen from the insets of Fig. 1(a), the full width at half maximum (FWHM) for the NiO (111) and Ni (111) diffraction peaks are 0.203° and 1.671° , respectively, demonstrating that the NiO film has a good crystallization quality. Furthermore, the in-plane crystallographic orientation between NiO, Ni, and PIN-PMN-PT is examined by XRD φ scans. In Fig. 1(b), the diffraction peaks for NiO appear at every 120° , proving that the NiO film has an in-plane threefold symmetry, consistent with the lattice symmetry of NiO (111) planes. However, the sixfold symmetrical diffraction peaks for the Ni phase are inconsistent with the threefold symmetry of Ni (111) planes, suggesting that the Ni unit cells have two in-plane lattice arrangement modes on the PIN-PMN-PT (111) plane, as schematically illustrated in Fig. 1(c). Therefore, the in-plane crystallographic relationships between the NiO–Ni film and the PIN-PMN-PT (111) substrate can be written as $[2\text{--}1\text{--}1]\text{NiO}/\text{Ni} \parallel [2\text{--}1\text{--}1]\text{PIN-PMN-PT}$, $[0\text{--}11]\text{NiO}/\text{Ni} \parallel [0\text{--}11]\text{PIN-PMN-PT}$.

Figure 1(d) records a symmetric butterfly like strain vs electric field (ε – E) curve and a square-like polarization vs electric field (P – E) hysteresis loop, which imply that the PIN-PMN-PT (111) substrates have excellent ferroelectric properties. The ferroelectric domain-switching properties of the PIN-PMN-PT (111) substrates are observed directly by piezoresponse force microscopy (PFM) shown in Fig. 1(e). When a $\pm 6\text{ V}$ voltage is applied to the PFM tip, the FE domains of a 0.1 mm thick PIN-PMN-PT crystal can be turn up or switch down toward the $[111]$ or $[-1\text{--}1\text{--}1]$ direction, leading to a clear contrast between the outer and inner squares. The atomic force microscopy (AFM) image, as shown in Fig. 1(f), reveals that the NiO–Ni film has a root mean square roughness of 4.9 nm . The existence of the Ni phase and in-plane epitaxial relationships of the NiO–Ni/PIN-PMN-PT heterostructure are revealed by high-resolution TEM (HRTEM). The thickness of the grown NiO–Ni film is determined as $\sim 95\text{ nm}$ [inset in Fig. 2(b)]. As shown by the area above the interface in Fig. 2(a), the lattice spacings of 0.24 nm and 0.21 nm correspond to the (111) and (200) planes of NiO, respectively, which also manifests that the growth direction of NiO films is (111)–

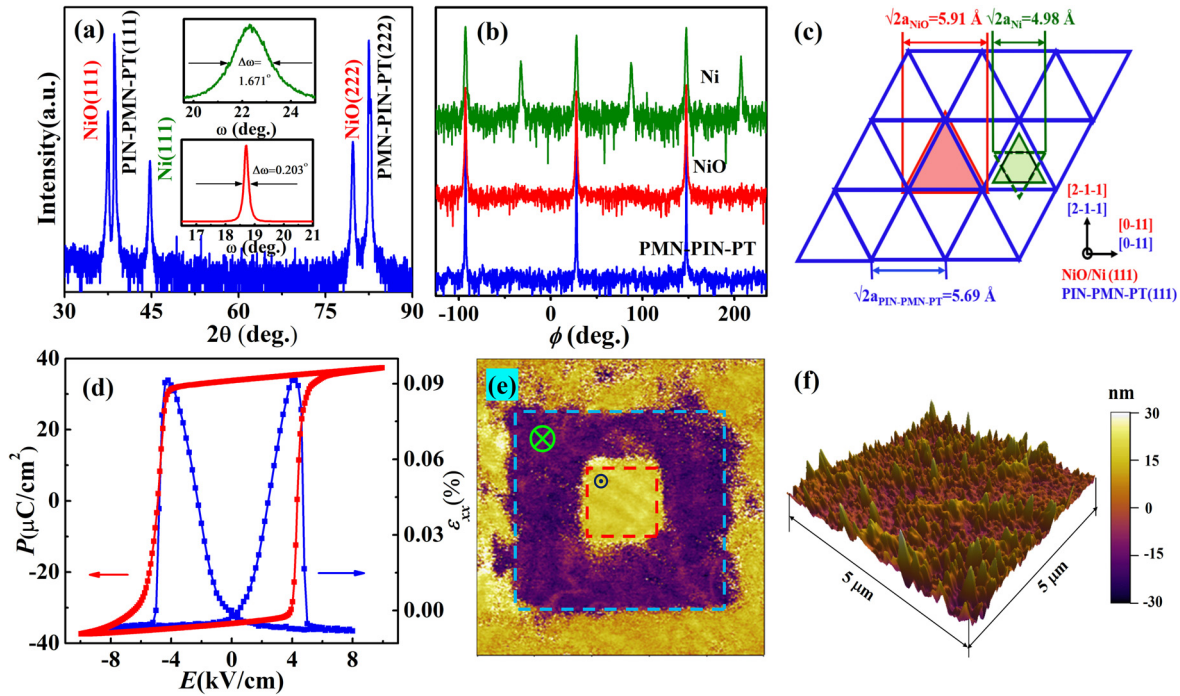


FIG. 1. (a) XRD θ - 2θ scan pattern for the NiO-Ni/PIN-PMN-PT structure; the insets show the XRD rocking curves taken on the NiO (111) (lower panel) and Ni (111) (upper panel) diffraction peaks. (b) XRD ϕ scan patterns taken on the NiO (200), Ni (200), and PIN-PMN-PT (200) diffraction peaks, respectively. (c) Schematic illustration of in-plane lattice arrangements of NiO and Ni unit cells on the PIN-PMN-PT (111) substrate. (d) Polarization and in-plane strain as a function of the bipolar electric field for a PIN-PMN-PT (111) substrate. (e) The electric-field-induced domain evolution of the PIN-PMN-PT (111) substrates. (f) The AFM image of the NiO-Ni film.

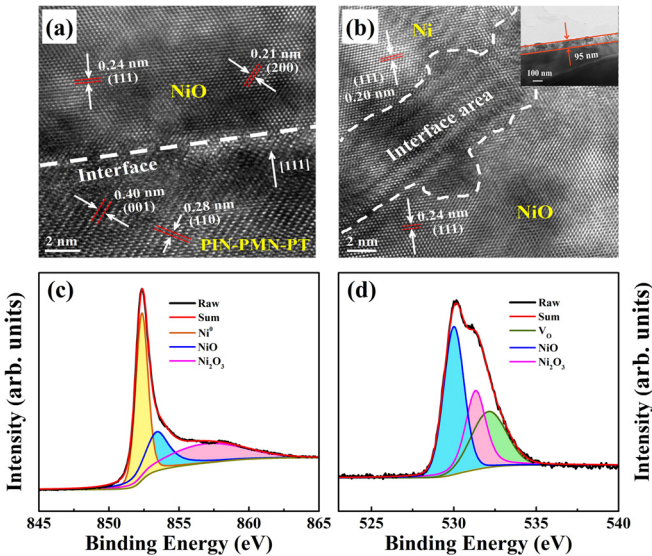


FIG. 2. (a) High-resolution TEM image of the NiO-Ni/PIN-PMN-PT structure. (b) Magnified HRTEM image to show Ni phases; the inset; cross-sectional TEM image of the NiO-Ni/PIN-PMN-PT structure. (c) Ni 2p XPS spectra of NiO-Ni films. (d) O 1s XPS spectra of NiO-Ni films.

oriented. Furthermore, the Ni phase is directly observed in the selected HRTEM image displayed in Fig. 2(b). The crystallographic orientation of the Ni phase is the same as that of the NiO film, in agreement with heteroepitaxial results shown in Figs. 1(a) and 1(b).

In order to further investigate the chemical valence states of Ni and O elements, Fig. 2(c) depicts the XPS depth profiling analyses of the Ni element. The core-level XPS spectra of Ni 2p_{3/2} can be divided into three peaks by Gaussian-Lorentzian fitting. The orange fitting peak [Fig. 2(c)] at the binding energy of 852.3 eV is attributed to the metallic Ni⁰ phase, consistent with some reported works.^{29,32} The blue and magenta peaks at the binding energy of 853.3 eV and 856.8 eV arise from NiO and Ni₂O₃, respectively. Meanwhile, Fig. 2(d) shows O 1s core level binding energy in the NiO films, and the three subpeaks at 530.0 eV, 531.3 eV, and 532.1 eV correspond to the lattice O²⁻ from NiO and Ni₂O₃, and oxygen vacancy V_O, respectively.³³ Based on the principles of defect chemistry, the transformation of lattice O²⁻ into V_O will create two electrons, which may be trapped by Ni³⁺ and Ni²⁺ cations to form Ni⁰ for charge neutrality as expressed by the following equations.³⁴ This evidence may account for the presence of the metallic Ni⁰ phase in the NiO matrix, which influences the electrical and magnetic transport properties of NiO-Ni composite films, as will be discussed in the following discussion,

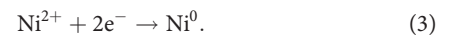
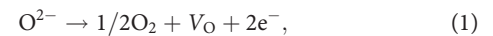


Figure 3(a) shows the resistance (R) of the NiO–Ni composite film measured by sweeping bipolar electric fields at $T = 300$ K (as schematically illustrated in Fig. S2, [supplementary material](#)). The relative resistance change $\Delta R/R$ is defined as $\Delta R/R = [R(P_r^-) - R(P_r^+)]/R(P_r^+)$, where $R(P_r^+)$ and $R(P_r^-)$ are the resistance of the NiO–Ni film under the positive and negative polarization states of PMN–PT without the application of electric fields, respectively. Note that the R – E loop exhibits a rectangular shape, similar to the shape of the P – E loop of the PIN–PMN–PT substrate [Fig. 1(d)], indicating that the interfacial charge effect plays the key role in determining the room temperature resistance switching behaviors. The maximum $\Delta R/R$ reaches 470% at $T = 300$ K. This value greatly exceeds (~ 400 times) those reported on some heterostructures that modulated by the lattice strain effect.^{11,12,35}

To further investigate the resistance switching mechanism, the carrier density of NiO–Ni films for the two polarization states [Figs. 3(c) and 3(d)] is measured using the van der Pauw configuration at $T = 300$ K. As shown in Fig. 3(b), the negative slopes of the Hall resistance vs magnetic field curves show that the NiO–Ni film deposited in high vacuum is an n -type semiconductor. In fact, the conduction type of the NiO film depends largely on the dominant defect type in the films prepared under different deposition conditions.^{34,36} The n -type conducting behavior here can be explained by the existence of oxygen vacancies shown by XPS results [Fig. 2(d)]. Furthermore, the significant discrepancy of slopes proves that the carrier densities are distinctly different for the two polarization states, i.e., $1.4 \times 10^{18} \text{ cm}^{-3}$ for

the P_r^+ state and $2.1 \times 10^{17} \text{ cm}^{-3}$ for the P_r^- state. Thus, together with the rectangular R – E curve, it can be concluded that the resistance switching behaviors are decisively modulated by the interfacial charge effect.

Figures 3(c) and 3(d) show the schematic illustrations for the polarization switching of the PIN–PMN–PT substrate. When a positive/negative electric field is applied to substrates, negative/positive polarization charges are accumulated at the top surface of PIN–PMN–PT, which attract holes/electrons to the interface region, leading to an increase/decrease in the electron carrier density and thus a decrease/increase in the resistance of the film. Meanwhile, the increase in electron carriers in the P_r^+ state may change a small portion of Ni^{2+} ions to the metallic Ni phase that is able to reduce the resistance of the film.²⁷ Furthermore, the interfacial charge effect is also supported by *in situ* XRD θ – 2θ scan results shown in Fig. 3(e), where the diffraction peaks remain unchanged upon the polarization state switching from P_r^+ to P_r^- , providing robust evidence that no additional remnant strain is induced in the film upon polarization switching. Taking advantage of the nonvolatile manipulation behavior, two reversible and nonvolatile resistance states, i.e., high resistance state and low resistance state, have been achieved at room temperature by applying pulsed electric fields $\pm 6 \text{ kV cm}^{-1}$ to the PIN–PMN–PT substrate [Fig. 3(f)].

The variations of the carrier density induced by polarization switching also influence the magnetotransport properties of the NiO–Ni films. Figure 4(a) shows the magnetoresistance (MR) vs

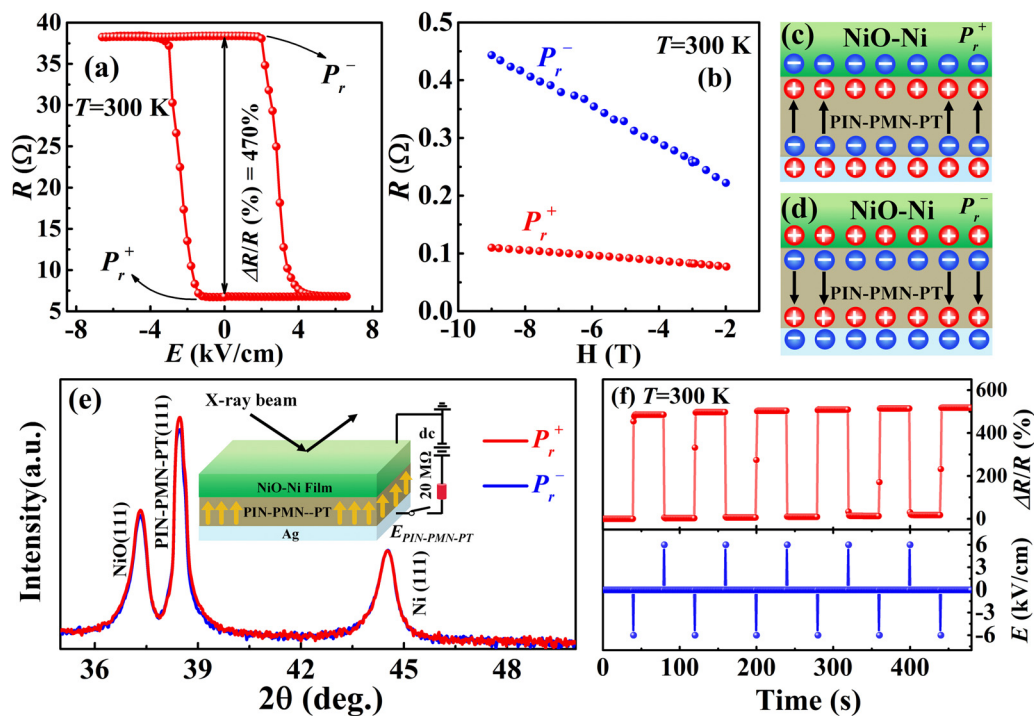


FIG. 3. (a) The resistance (R) of the NiO–Ni film as a function of bipolar electric fields applied to the PIN–PMN–PT substrates. (b) Hall resistance of the NiO–Ni film as a function of the magnetic field when the PIN–PMN–PT substrate was in the positive poling state P_r^+ and negative poling state P_r^- , respectively. (c) and (d) Schematic illustrations for the accumulation and depletion of electron carriers in the NiO–Ni film upon positive and negative poling of the PIN–PMN–PT substrate. (e) Out-of-plane XRD θ – 2θ scan patterns of the NiO–Ni/PIN–PMN–PT heterostructure under two polarization states; the inset is the schematic illustration for *in situ* XRD measurements. (f) Nonvolatile resistance switching of the NiO–Ni film by a sequence of pulse electric fields at $T = 300$ K.

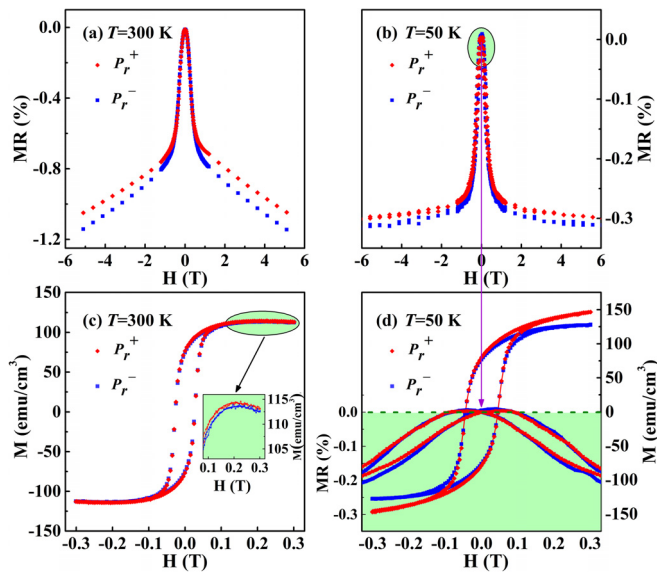


FIG. 4. Magnetoresistance (MR) of the NiO-Ni film as a function of the magnetic field (H) for the P_r^+ (red) and P_r^- (blue) polarization states at (a) $T = 300$ K and (b) $T = 50$ K. Magnetic hysteresis loops of the NiO-Ni film for the P_r^+ and P_r^- states at (c) $T = 300$ K and (d) $T = 50$ K. The inset in (c) shows the enlarged view of the magnetization for P_r^+ and P_r^- at $H > 0.1$ T. The colored area in (d) is the enlarged view of the butterfly shaped MR- H curve in the low-field region in (b).

magnetic field H for the NiO-Ni film for the P_r^+ and P_r^- states of PIN-PMN-PT at 300 K. Here, MR is defined as $MR = [R(H) - R(0)]/R(0)$, where $R(H)$ and $R(0)$ refer to the resistance of the NiO-Ni film in the presence and absence of a magnetic field H . At room temperature, the sharp decrease in the negative MR in the low-field region ($H \leq 1$ T) may be related to the spin-scattering related tunneling effect of Ni/NiO/Ni upon application of magnetic fields.³⁷ In the high-field region ($H > 1$ T), the MR for both polarization states decreases gently with the increasing magnetic field, which could be explained by the reduced magnetic scattering of conducting electrons.³⁸ The MR values for P_r^+ are smaller than those for P_r^- ($H > 1$ T) in these measured temperatures, and this is presumably caused by different electron carrier densities between the two polarization states.³⁹ Intriguingly, a butterfly shaped MR- H curve in the low-field region is observed in Fig. 4(b) and magnified in Fig. 4(d). The MR- H curve couples with the M - H one, and the peak position of MR locates at the coercive field of the M - H loop. These phenomena demonstrate that the magnetotransport properties of NiO-Ni films could also be modulated by the interfacial charge effect.

Figure 4(c) shows that the NiO-Ni composite films exhibit a typical magnetic hysteresis loop for both the P_r^+ and P_r^- states. In this work, because NiO is antiferromagnetic²⁷ and Ni_2O_3 is nonmagnetic⁴⁰ the ferromagnetism of NiO-Ni films can only originate from the metallic Ni. It can be seen from the inset that the saturation magnetization M_s for the P_r^+ state is slightly larger than that for the P_r^- state. A complete M - H hysteresis loop measured at $T = 50$ K is presented in Fig. 4(d) from which one may find an enhanced ferromagnetism at low temperature. Particularly, the relative change of M_s , $\Delta M_s/M_s = [M_s(P_r^+) - M_s(P_r^-)]/M_s(P_r^-)$, up to 15% is achieved at

TABLE I. The carrier densities at 300 and 50 K with different polarization states of PIN-PMN-PT.

	$n(P_r^+) \text{ (cm}^{-3}\text{)}$	$n(P_r^-) \text{ (cm}^{-3}\text{)}$	$\Delta n [n(P_r^+) - n(P_r^-)] \text{ (cm}^{-3}\text{)}$
300 K	1.4×10^{18}	2.1×10^{17}	1.19×10^{18}
50 K	9.3×10^{18}	1.7×10^{18}	7.6×10^{18}

50 K. This significant modulation on M_s is possibly attributed to two reasons. On one hand, the greater difference of M_s can be ascribed to the larger absolute difference in carrier density ($7.6 \times 10^{18} \text{ cm}^{-3}$) between the two polarization states (Fig. S3, [supplementary material](#)), as compared with the corresponding value at 300 K ($1.19 \times 10^{18} \text{ cm}^{-3}$). The change of carrier density could influence the conductivity of the Ni phase, which further affects M_s . On the other hand, upon switching the polarization state from the P_r^- state to the P_r^+ state, more electron carriers (compared to the results at 300 K, Table I) are induced due to the ferroelectric field effect. This may convert a small portion of Ni^{2+} ions to the metallic Ni^0 , resulting in the increase in M_s [Fig. 4(d)]. A similar phenomenon has also been observed by Kang *et al.* who applied ionic liquid pretreatment to the NiO film to convert a portion of Ni^{2+} to metallic nickel (Ni^0) and thus achieved large-magnitude magnetic modulation.²⁷

In summary, we prepared heteroepitaxial NiO-Ni composite films on PIN-PMN-PT (111) single-crystal substrates with a single phase NiO ceramic target by the pulse laser deposition technique. The high vacuum deposition process causes the formation of oxygen deficiency and Ni metal, resulting in n -type electrical conductivity and ferromagnetism of the composite film at room temperature. Upon switching the polarization states of PIN-PMN-PT, two reversible and nonvolatile resistance states with $\Delta R/R \sim 470\%$ are obtained for the composite films, and an appreciable charge-mediated modulation of the magnetization has been achieved at 50 K. Our work not only implies that the electrical and/or magnetic properties of similar composite films (e.g., FeO-Fe, CoO-Co, TiO-Ti, and CrO-Cr) may be modified by the injection or removal of charge carriers using ferroelectric or dielectric gating but also offers a simple way to design semiconducting ferromagnetic composite film/FE structures for nonvolatile memory and spintronic device applications.

See the [supplementary material](#) for the schematic of the experimental setup for the measurements of the electric field-induced in-plane strain in the PIN-PMN-PT (111) substrate and the measurements of the Hall effect via the van der Pauw method and also the schematic illustration for the measurements of the resistance vs electric field under P_r^+ and P_r^- states and the Hall resistance of the NiO-Ni film for P_r^+ and P_r^- states at $T = 50$ K.

This work was supported by the National Natural Science Foundation of China (Grant Nos. 11974155, 51872278, and 11974250) and the Science and Technology Commission of Shanghai Municipality (Grant No. 19070502800).

DATA AVAILABILITY

The data that support the findings of this study are available from the corresponding author upon reasonable request.

REFERENCES

- ¹Y. Sharma, P. Misra, S. P. Pavunny, and R. S. Katiyar, *Appl. Phys. Lett.* **104**, 073501 (2014).
- ²X. Y. Zhao, J. H. Wen, B. Yang, H. C. Zhu, Q. Q. Cao, D. H. Wang, Z. H. Qian, and Y. W. Du, *ACS Appl. Mater. Interfaces* **9**, 36038 (2017).
- ³S. Zhang, Y. G. Zhao, P. S. Li, J. J. Yang, S. Rizwan, J. X. Zhang, J. Seidel, T. L. Qu, Y. J. Yang, Z. L. Luo, Q. He, T. Zou, Q. P. Chen, J. W. Wang, L. F. Yang, Y. Sun, Y. Z. Wu, X. Xiao, X. F. Jin, J. Huang, C. Gao, X. F. Han, and R. Ramesh, *Phys. Rev. Lett.* **108**, 137203 (2012).
- ⁴R. K. Zheng, Y. Jiang, Y. Wang, C. L. Choy, and H. S. Luo, *Phys. Rev. B* **79**, 174420 (2009).
- ⁵S. Trommler, R. Hühne, K. Iida, P. Pahlke, S. Haindl, L. Schultz, and B. Holzapfel, *New J. Phys.* **12**, 103030 (2010).
- ⁶M. D. Biegalski, D. H. Kim, S. Choudhury, L. Q. Chen, H. M. Christen, and K. Dörr, *Appl. Phys. Lett.* **98**, 142902 (2011).
- ⁷F. F. Wang, D. Liu, Z. B. Chen, Z. H. Duan, Y. Zhang, D. Z. Sun, X. Y. Zhao, W. Z. Shi, R. K. Zheng, and H. S. Luo, *J. Mater. Chem. C* **5**, 9115 (2017).
- ⁸Z. G. Wang, Y. Zhang, R. Viswan, Y. X. Li, H. S. Luo, J. F. Li, and D. Viehland, *Phys. Rev. B* **89**, 035118 (2014).
- ⁹J. M. Yan, Z. X. Xu, T. W. Chen, M. Xu, C. Zhang, X. W. Zhao, W. Y. Zhao, and R. K. Zheng, *ACS Appl. Mater. Interfaces* **11**, 9548–9556 (2019).
- ¹⁰W. J. Jie, Y. Y. Hai, and N. Y. Chan, *J. Phys. Chem. C* **117**, 13747 (2013).
- ¹¹M. Zheng, H. Ni, Y. P. Qi, W. Y. Huang, J. L. Zeng, and J. Gao, *Appl. Phys. Lett.* **110**, 182403 (2017).
- ¹²J. M. Yan, M. Xu, T. W. Chen, M. M. Yang, F. Liu, L. Guo, Z. X. Xu, G. Y. Gao, H. S. Luo, and R. K. Zheng, *Phys. Rev. Appl.* **11**, 034037 (2019).
- ¹³W. Zhang, M. M. Yang, X. Liang, H. W. Zheng, Y. Wang, G. L. Yuan, W. F. Zhang, H. S. Luo, and R. K. Zheng, *Nano Energy* **18**, 315–324 (2015).
- ¹⁴B. W. Zhi, G. Y. Gao, H. R. Xu, F. Chen, X. L. Tan, P. F. Chen, L. F. Wang, and W. B. Wu, *ACS Appl. Mater. Interfaces* **6**, 4603–4608 (2014).
- ¹⁵Y. Lee, Z. Q. Liu, J. T. Heron, J. D. Clarkson, J. Hong, M. D. Biegalski, U. Aschauer, S. L. Hsu, M. E. Nowakowski, J. Wu, H. M. Christen, S. Salahuddin, J. B. Bokor, N. A. Spaldin, D. G. Schlom, and R. Ramesh, *Nat. Commun.* **6**, 5959 (2015).
- ¹⁶Q. X. Zhu, M. M. Yang, M. Zheng, R. K. Zheng, L. J. Guo, Y. Wang, and J. X. Zhang, *Adv. Funct. Mater.* **25**, 1111–1119 (2015).
- ¹⁷Z. X. Xu, J. M. Yan, M. Xu, L. Guo, T. W. Chen, G. Y. Gao, M. Zheng, J. X. Zhang, Y. Wang, and R. K. Zheng, *ACS Appl. Mater. Interfaces* **10**, 32809–32817 (2018).
- ¹⁸Y. Y. Wang, X. Zhou, C. Song, Y. N. Yan, S. M. Zhou, G. Y. Wang, C. Chen, F. Zeng, and F. Pan, *Adv. Mater.* **27**, 3196 (2015).
- ¹⁹T. Maruyama, Y. Shiota, T. Nozaki, K. Ohta, N. Toda, M. Mizuguchi, A. A. Tulapurkar, T. Shinjo, M. Shiraishi, S. Mizukami, Y. Ando, and Y. Suzuki, *Nat. Nanotechnol.* **4**, 158 (2009).
- ²⁰T. Story, R. R. Galazka, R. B. Frankel, and P. A. Wolff, *Phys. Rev. Lett.* **56**, 777 (1986).
- ²¹A. J. Behan, A. Mokhtari, H. J. Blythe, D. Score, X. H. Xu, J. R. Neal, A. M. Fox, and G. A. Gehring, *Phys. Rev. Lett.* **100**, 047206 (2008).
- ²²Y. Matsumoto, M. Murakami, T. Shono, T. Hasegawa, T. Fukumura, M. Kawasaki, P. Ahmet, T. Chikyow, S. Koshihara, and H. Koinuma, *Science* **291**, 854 (2001).
- ²³S. B. Ogale, R. J. Choudhary, J. P. Buban, S. E. Lofland, S. R. Shinde, S. N. Kale, V. N. Kulkarni, J. Higgins, C. Lanci, J. R. Simpson, N. D. Browning, S. D. Sarma, H. D. Drew, R. L. Greene, and T. Venkatesan, *Phys. Rev. Lett.* **91**, 077205 (2003).
- ²⁴B. J. Al, L. Zeidan, A. Khalaf, and R. S. Awad, *Chem. Phys.* **516**, 116–124 (2019).
- ²⁵P. M. Ponnusamy, S. Agilan, N. Muthukumarasamy, and D. Velauthapillai, *Z. Phys. Chem.* **230**, 1185–1197 (2016).
- ²⁶S. N. Kale, S. B. Ogale, S. R. Shinde, M. Sahasrabudhe, V. N. Kulkarni, R. L. Greene, and T. Venkatesan, *Appl. Phys. Lett.* **82**, 2100 (2003).
- ²⁷X. Kang, Y. J. Gao, L. F. Liu, W. Chen, and X. Zhao, *Appl. Phys. Lett.* **115**, 103501 (2019).
- ²⁸Y. Luo, D. Zhao, Y. Zhao, F. K. Chiang, P. Chen, M. Guo, N. Luo, X. Jiang, P. Miao, Y. Sun, A. Chen, Z. Lin, J. Li, W. Duan, J. Cai, and Y. Wang, *Nanoscale* **7**, 642 (2015).
- ²⁹J. P. Domann, W. Y. Sun, L. T. Schelhas, and G. P. Carman, *J. Appl. Phys.* **120**, 143904 (2016).
- ³⁰Z. X. Xu, J. M. Yan, M. Xu, L. Guo, T. W. Chen, G. Y. Gao, and Y. Wang, *Appl. Phys. Lett.* **113**, 223504 (2018).
- ³¹S. Fujime, M. Murakami, and E. Hirahara, *J. Phys. Soc. Jpn.* **16**, 183–186 (1961).
- ³²L. J. Wei, Z. Z. Hu, G. X. Du, Y. Yuan, J. Wang, H. Q. Tu, B. You, S. M. Zhou, J. T. Qu, H. W. Liu, R. K. Zheng, Y. Hu, and J. Du, *Adv. Mater.* **30**, 1801885 (2018).
- ³³Z. B. Fang, S. U. Rehman, M. Z. Sun, Y. P. Yuan, S. W. Jin, and H. Bi, *J. Mater. Chem. A* **6**, 21131 (2018).
- ³⁴R. Molaei, R. Bayati, and J. Narayan, *Cryst. Growth Des.* **13**, 5459–5465 (2013).
- ³⁵M. Liu, J. Hoffman, J. Wang, J. X. Zhang, B. N. Cheeseman, and A. Bhattacharya, *Sci. Rep.* **3**, 1876 (2013).
- ³⁶C. Park, J. Kim, K. Lee, S. K. Oh, H. J. Kang, and N. S. Park, *Appl. Sci. Convergence Technol.* **24**, 72–76 (2015).
- ³⁷S. Maekawa and U. Gafvert, *IEEE Trans. Magn.* **2**, 707 (1982).
- ³⁸Y. An, Y. Ren, D. Yang, Z. Wu, and J. Liu, *J. Phys. Chem. C* **119**, 4414–4421 (2015).
- ³⁹M. Xu, J. M. Yan, L. Guo, H. Wang, Z. X. Xu, M. Y. Yan, Y. L. Lu, G. Y. Gao, X. G. Li, H. S. Luo, Y. Chai, and R. K. Zheng, *ACS Appl. Mater. Interfaces* **11**, 32449–32459 (2019).
- ⁴⁰B. C. Wang, J. L. Zhang, T. Wang, L. Qiao, and F. S. Li, *J. Alloys Compd.* **567**, 21–25 (2013).